


Cite this: *RSC Adv.*, 2022, **12**, 2292

## First-principles study on optoelectronic properties of $\text{Cs}_2\text{PbX}_4$ – $\text{PtSe}_2$ van der Waals heterostructures†

Xue Li,<sup>ab</sup> Liyuan Wu,<sup>id,\*c</sup> Shuying Cheng,<sup>d</sup> Changcheng Chen,<sup>id,e</sup> and Pengfei Lu<sup>id,\*ab</sup>

In order to achieve low-cost, high efficiency and stable photoelectric devices, two-dimensional (2D) inorganic halide perovskite photosensitive layers need to cooperate with other functional layers. Here, we investigate the structure, stability and optical properties of perovskite and transition metal dichalcogenide (TMD) heterostructures using first-principles calculations. Firstly,  $\text{Cs}_2\text{PbX}_4$ – $\text{PtSe}_2$  ( $\text{X} = \text{Cl}, \text{Br}, \text{I}$ ) heterostructures are stable because of negative interface binding energy. With the halogen varying from Cl to I, the interface binding energies of  $\text{Cs}_2\text{PbX}_4$ – $\text{PtSe}_2$  heterostructures decrease rapidly. 2D  $\text{Cs}_2\text{PbCl}_4$ – $\text{PtSe}_2$ ,  $\text{Cs}_2\text{PbBr}_4$ – $\text{PtSe}_2$  and  $\text{Cs}_2\text{PbI}_4$ – $\text{PtSe}_2$  heterostructures have an indirect bandgap with the value of 1.28, 1.02, and 1.29 eV, respectively, which approach the optimal bandgap (1.34 eV) for solar cells. In the contact state, the electrons transfer from the  $\text{PtSe}_2$  monolayer to  $\text{Cs}_2\text{PbX}_4$  monolayer and only the  $\text{Cs}_2\text{PbBr}_4$ – $\text{PtSe}_2$  heterostructure maintains the type-II band alignment. The  $\text{Cs}_2\text{PbBr}_4$ – $\text{PtSe}_2$  heterostructure has the strongest charge transfer among the three  $\text{Cs}_2\text{PbX}_4$ – $\text{PtSe}_2$  heterostructures because it has the lowest tunnel barrier height ( $\Delta T$ ) and the highest potential difference value ( $\Delta EP$ ). Furthermore, the light absorption coefficient of  $\text{Cs}_2\text{PbX}_4$ – $\text{MSe}_2$  heterostructures is at least two times higher than that of monolayer 2D inorganic halide perovskites. With the halogen varying from Cl to I, the light absorption coefficients of the  $\text{Cs}_2\text{PbX}_4$ – $\text{PtSe}_2$  heterostructures increase rapidly in the visible region. Above all, the  $\text{Cs}_2\text{PbX}_4$ – $\text{MSe}_2$  heterostructures have broad application prospects in photodetectors, solar cells and other fields.

Received 23rd November 2021

Accepted 28th December 2021

DOI: 10.1039/d1ra08574c

[rsc.li/rsc-advances](http://rsc.li/rsc-advances)

## Introduction

In recent years, halide perovskites have attracted much attention because of their promising optoelectronic applications such as in photodetectors, light-emitting diodes (LEDs), and solar cells.<sup>1–3</sup> The power conversion efficiency (PCE) of the halide perovskite solar cells has increased continuously from 3.8% to 25.6%.<sup>4,5</sup> Early research mainly focused on lead-based three-dimensional (3D) halide perovskite materials with a general formula  $\text{ABX}_3$  due to their excellent optoelectronic properties. However, the instability of the 3D hybrid perovskite

perovskites in the environment with high humidity or high-temperature is a major challenge for their large-scale applications.<sup>6</sup> Therefore, a substantial part of the current research efforts is dedicated to improve the stability of perovskite solar cells by searching for alternative materials with comparable optoelectronic properties with the 3D hybrid halide perovskites but high materials stability.<sup>7–11</sup>

Two-dimensional (2D) inorganic halide perovskites with excellent moisture resistance and stability have been exploring for optoelectronic devices.<sup>12</sup> In theoretical calculations, Bala *et al.* revealed objective laws that the band gap and optical property of multilayered 2D  $\text{Cs}_{n+1}\text{Pb}_n\text{X}_{3n+1}$  ( $\text{X} = \text{Cl}, \text{Br}, \text{I}$ ) perovskite vary with layer  $n$ .<sup>13</sup> Swarnkar *et al.* have shown the PCE of A- $\text{CsPbI}_3$  quantum dots exceed 10% and they are stable under environmental conditions.<sup>14</sup> In order to achieve low-cost, high efficiency, stable photoelectric devices, 2D inorganic halide perovskites photoactive layers need to cooperate with other functional layers.<sup>15–20</sup> Two-dimensional materials, such as graphene, MXene and black phosphorus (BP) have unique electronic, thermal, mechanical and photonic properties, which are widely used as functional layers for 2D perovskite photo-electric equipment.<sup>21–27</sup> Especially, two-dimensional transition metal dichalcogenides (TMDs) as the functional layers can significantly improve the efficiency of 2D inorganic halide perovskite optoelectronic devices.<sup>28,29</sup>

<sup>a</sup>State Key Laboratory of Information Photonics and Optical Communications, Beijing University of Posts and Telecommunications, Beijing 100876, China

<sup>b</sup>School of Electronic Engineering, Beijing University of Posts and Telecommunications, Beijing 100876, China. E-mail: photon@bupt.edu.cn

<sup>c</sup>CAS Key Laboratory for Biomedical Effects of Nanomaterials and Nanosafety, Institute of High Energy Physics, Chinese Academy of Sciences, Beijing 100049, China. E-mail: wuly2018@gmail.com

<sup>d</sup>School of Information Management, Beijing Information Science & Technology University, Beijing 100085, China

<sup>e</sup>School of Science, Xi'an University of Architecture and Technology, Xi'an 710055, Shaanxi, China

† Electronic supplementary information (ESI) available: The band structures of monolayer  $\text{Cs}_2\text{PbX}_4$  and  $\text{PtSe}_2$  by different calculation functional. See DOI: 10.1039/d1ra08574c



As an emerging TMDs material,  $\text{PtSe}_2$  exhibits excellent optical, electrical, stabilized and mechanical properties. Single-crystal monolayer  $\text{PtSe}_2$  thin films have been successfully fabricated with an indirect bandgap of 1.2 eV.<sup>30</sup> The bandgap of  $\text{PtSe}_2$  decreases when the layer number of  $\text{PtSe}_2$  and the thickness of  $\text{PtSe}_2$  increase, which is an effective way to achieve the metal to semiconductor transition.<sup>31</sup> The bandgap of  $\text{PtSe}_2$  is widely tunable, so it can be effectively responsive to near-infrared light compared with that of BP.<sup>32</sup> Therefore,  $\text{PtSe}_2$  exhibits a promising material for optoelectronic device applications such as photo-detectors, field-effect transistors (FET) and halide perovskite solar cells.<sup>33</sup> For example, Zeng *et al.* revealed that  $\text{PtSe}_2/\text{GaAs}$  heterostructure has a broad sensitivity range of illumination.<sup>34</sup>  $\text{PtSe}_2/\text{FA}_{0.85}\text{Cs}_{0.15}\text{PbI}_3$  heterostructure photodetector has a wide range of optical response and photosensitive characteristics such as fast responsivity, high  $I_{\text{light}}/I_{\text{dark}}$  ratio and decent specific detectivity at zero bias.<sup>35</sup> However, interface electronic transfer and band alignment of  $\text{Cs}_2\text{PbX}_4\text{--PtSe}_2$  ( $\text{X} = \text{Cl}, \text{Br}, \text{I}$ ) heterostructures are not studied theoretically. It's worth to reveal the effect of halide elements on  $\text{Cs}_2\text{PbX}_4\text{--PtSe}_2$  heterostructures, which can promote the development of 2D inorganic halide perovskite and TMDs optoelectronic applications.

Herein, we constructed the 2D inorganic halide perovskite  $\text{Cs}_2\text{PbX}_4$  and monolayer  $\text{PtSe}_2$  heterostructures and explored optoelectronic properties, the charge transfer and band alignment *via* first-principles calculations. At first, we used DFT-D3 method to optimize the heterostructures and studied their geometric structures and stability. Then, we analysed the band alignment type and the work-function of heterostructures with different halide elements. Next, we calculated plane-averaged electrostatic potential and charge density difference to explore the charge transfer mechanism. Finally, we calculated the optical absorption coefficients of monolayer  $\text{PtSe}_2$ ,  $\text{Cs}_2\text{PbX}_4$  and heterostructures  $\text{Cs}_2\text{PbX}_4\text{--PtSe}_2$ . Constructing  $\text{Cs}_2\text{PbX}_4\text{--PtSe}_2$  heterostructures can effectively enhance the optical properties for 2D inorganic halide perovskites.

## Computational details

All calculations were performed in the framework of density functional theory (DFT) implemented in the Vienna Ab initio Simulation Package (VASP) code with the projected augmented wave (PAW) method.<sup>36,37</sup> Perdew–Burke–Ernzerhof (PBE) functional was employed treat the electron exchange–correlation interaction.<sup>38</sup> In order to optimize the atomic structure for correcting the van der Waals (vdW) interaction, we used DFT-D3 method of Grimme and chose a  $3 \times 3 \times 1$  Monkhorst–Pack  $k$ -point meshes for the Brillouin zone.<sup>39,40</sup> The cutoff energy of the plane-wave was set to 450 eV and convergence for total energy is  $1 \times 10^{-4}$  eV was set in the self-consistent calculations. All atoms were fully relaxed until the total forces converge to 0.05 eV  $\text{\AA}^{-1}$ . A vacuum space of 20  $\text{\AA}$  was set to avoid interaction between the model's periodic images. The Heyd–Scuseria–Ernzerhof (HSE) hybrid functional is applied for electronic structure calculation of 2D inorganic halide perovskites to correct the band gaps.<sup>41,42</sup> The spin–orbit coupling (SOC) were also considered because of the existence of the heavy elements in Pb.<sup>43</sup>

To study the stability of the  $\text{Cs}_2\text{PbX}_4\text{--PtSe}_2$  heterostructures, we calculated interface binding energy by the following formula:

$$E_b = (E_{\text{heter.}} - E_{\text{Cs}_2\text{PbX}_4} - E_{\text{PtSe}_2})/A \quad (1)$$

where  $A$  represents the interfacial area of  $\text{Cs}_2\text{PbX}_4\text{--PtSe}_2$  heterostructures,  $E_{\text{heter.}}$ ,  $E_{\text{Cs}_2\text{PbX}_4}$ ,  $E_{\text{PtSe}_2}$  are the total energy of heterostructures  $\text{Cs}_2\text{PbX}_4\text{--PtSe}_2$ , monolayer  $\text{Cs}_2\text{PbX}_4$  and  $\text{PtSe}_2$ , respectively.

Plane-averaged charge density difference  $\Delta\rho$  which can be quantitatively calculated as the followed equation:

$$\Delta\rho(z) = \rho_{\text{heter.}} - \rho_{\text{Cs}_2\text{PbX}_4} - \rho_{\text{PtSe}_2} \quad (2)$$

where  $\rho_{\text{heter.}}$ ,  $\rho_{\text{Cs}_2\text{PbX}_4}$  and  $\rho_{\text{PtSe}_2}$  correspond to the plane-averaged charge density of heterojunctions  $\text{Cs}_2\text{PbX}_4\text{--PtSe}_2$ , monolayer  $\text{Cs}_2\text{PbX}_4$  and  $\text{PtSe}_2$ , respectively.

The 2D Mott–Wannier (MW) exciton binding energy ( $E_{\text{eb}}$ ) equation is as followed:

$$E_{\text{eb}} = 4 \frac{13.6\mu_{\text{ex}}}{m_0\epsilon^2} \text{ eV} \quad (3)$$

where  $\mu_{\text{ex}}$  is the effective exciton mass ( $\mu_{\text{ex}} = m_e m_h / (m_e + m_h)$ ),  $m_0$  is the electron mass, and  $\epsilon$  is the static dielectric constant. The effective masses of electron ( $m_e$ ) and hole ( $m_h$ ) are determined by the curvature of the energy band extremum.

The optical absorption coefficients are obtained from dielectric function, as the followed equation represented:

$$\alpha(\omega) = \left( \sqrt{2} \right) \omega \left[ \sqrt{\varepsilon_1(\omega)^2 + \varepsilon_2(\omega)^2} - \varepsilon_1(\omega) \right]^{1/2} \quad (4)$$

$$\varepsilon(\omega) = \varepsilon_1(\omega) + i\varepsilon_2(\omega) \quad (5)$$

where  $\alpha$ ,  $\omega$  correspond to the optical absorption coefficient, the angular frequency and the dielectric function  $\varepsilon(\omega)$  contains real part  $\varepsilon_1(\omega)$  and imaginary part  $\varepsilon_2(\omega)$ .

## Results and discussion

In recent years, 2D inorganic cubic phases of halide perovskites and 2D  $\text{PtSe}_2$  have been successfully synthesized, which attracted much attention due to the stability compared with 3D hybrid perovskite. The calculated lattice parameter of the monolayer cubic phase  $\text{Cs}_2\text{PbCl}_4$ ,  $\text{Cs}_2\text{PbBr}_4$ ,  $\text{Cs}_2\text{PbI}_4$  is 5.64  $\text{\AA}$ , 5.91  $\text{\AA}$ , 6.30  $\text{\AA}$ , as listed in Table 1, which agree well with both experimental and theoretical values.<sup>42,43</sup> Firstly, we chosen the (001) surface of  $\text{Cs}_2\text{PbX}_4$  ( $\text{X} = \text{Cl}, \text{Br}, \text{I}$ ) to construct the heterostructures, because it consists of alternating superposition of neutral planes  $[\text{PbI}_2]^0$  and  $[\text{CsI}]^0$ , which can effectively reduce dangling bonds.<sup>44,45</sup> In addition,  $[\text{CsI}]^0$  interface exhibits stronger charge transferring than  $[\text{PbI}_2]^0$ , therefore  $\text{Cs}_2\text{PbX}_4\text{--PtSe}_2$  heterostructures consist of the  $[\text{CsI}]^0$  plane of the monolayer  $\text{Cs}_2\text{PbX}_4$ .<sup>42</sup> In the  $Z$  direction, we use a large vacuum space of 20  $\text{\AA}$  to avoid the interlayer interaction. In order to find out the effect of halogen elements on  $\text{Cs}_2\text{PbX}_4\text{--PtSe}_2$  heterostructure, we firstly adopt the same heterostructure expansion



**Table 1** Optimized lattice parameters ( $a$  and  $b$ ) of monolayer  $\text{Cs}_2\text{PbX}_4$ , configuration, lattice mismatch, interlayer distance  $\Delta Z$  and interface formation energy  $E_b$  of the relaxed  $\text{Cs}_2\text{PbX}_4$ – $\text{PtSe}_2$  heterostructures

Heterostructures	Configuration	$a$ (Å)	$b$ (Å)	$\Delta Z$ (Å)	Mismatch (%)		$E_b$ (meV)	Mismatch (%)	
					$a = b$ (Å)	$a = b^a$ (Å)		$a$	$b$
$\text{Cs}_2\text{PbCl}_4$ – $\text{PtSe}_2$	$2 \times 2/2\sqrt{3} \times 3$	12.49	11.20	2.76	5.64	5.73	−6.32	7.25	0.03
	$\sqrt{10} \times \sqrt{5}/5 \times \sqrt{3}$	18.37	13.18	2.84			−7.78	2.68	3.66
$\text{Cs}_2\text{PbBr}_4$ – $\text{PtSe}_2$	$2 \times 2/2\sqrt{3} \times 3$	12.58	11.31	2.79	5.91	6.00	−11.30	4.86	0.02
	$\sqrt{10} \times \sqrt{5}/5 \times \sqrt{13}$	18.55	13.34	2.89			−46.07	0.30	1.27
$\text{Cs}_2\text{PbI}_4$ – $\text{PtSe}_2$	$2 \times 2/2\sqrt{3} \times 3$	12.86	11.33	2.91	6.30	6.40	−16.78	1.66	5.26
	$\sqrt{8} \times 2/5 \times \sqrt{13}$	18.31	13.23	2.88			−15.34	2.69	3.67

<sup>a</sup> Values with PBE are from ref. 39.

method, as shown in Fig. S1.† The unit cells of 2D  $\text{Cs}_2\text{PbX}_4$ – $\text{PtSe}_2$  are made up of  $2\sqrt{3} \times 3$  supercell of monolayer  $\text{PtSe}_2$  and  $2 \times 2$  supercell of monolayer  $\text{Cs}_2\text{PbX}_4$ . The optimized vertical interlayer distances of the  $\text{Cs}_2\text{PbCl}_4$ – $\text{PtSe}_2$ ,  $\text{Cs}_2\text{PbBr}_4$ – $\text{PtSe}_2$ ,  $\text{Cs}_2\text{PbI}_4$ – $\text{PtSe}_2$  heterostructures calculated with vdW force are 2.76 Å, 2.79 Å, and 2.91 Å, which increase gradually with the halogen varying from Cl to I. However, the optimized vertical interlayer distances of  $\text{Cs}_2\text{PbX}_4$ – $\text{PtSe}_2$  heterostructures calculated without vdW force are about 4 Å, so vdW force was considered in the optimization of  $\text{Cs}_2\text{PbX}_4$ – $\text{PtSe}_2$  heterostructures.

The interface binding energy ( $E_b$ ) of  $\text{Cs}_2\text{PbCl}_4$ – $\text{PtSe}_2$ ,  $\text{Cs}_2\text{PbBr}_4$ – $\text{PtSe}_2$  and  $\text{Cs}_2\text{PbI}_4$ – $\text{PtSe}_2$  interfaces is −6.32, −11.30 and −16.78 meV Å<sup>−2</sup>. The three  $E_b$  values are comparable to these of  $\text{CsPbI}_3/\text{MoS}_2$  (−21 meV Å<sup>−2</sup>) and  $\text{InSe}/\text{GaSe}$  (−18.25 meV Å<sup>−2</sup>), suggesting that  $\text{Cs}_2\text{PbX}_4$ – $\text{PtSe}_2$  heterostructures are stable in energy.<sup>46,47</sup> With the halogen varying from Cl to I, the interface binding energies of  $\text{Cs}_2\text{PbX}_4$ – $\text{PtSe}_2$  heterostructures decrease rapidly and heterostructures become more stable in energy due to the lower interface binding energy.<sup>48,49</sup> Above all, the interlayer distance ranging from 2.76 Å to 2.91 Å belong to vdW and small interface binding energy revealed that 2D  $\text{Cs}_2\text{PbX}_4$ – $\text{PtSe}_2$  heterostructures are formed by vdW contact. The lattice mismatches of the 2D  $\text{Cs}_2\text{PbCl}_4$ – $\text{PtSe}_2$ ,  $\text{Cs}_2\text{PbBr}_4$ – $\text{PtSe}_2$  and  $\text{Cs}_2\text{PbI}_4$ – $\text{PtSe}_2$  heterostructures in the  $a$  and  $b$  directions are less than 7.25%, 4.86% and 5.54%.

The lattice mismatch between two layers is usually required to be less than 5% to ensure the stability of heterojunctions, the unit cell of  $\text{Cs}_2\text{PbX}_4$ – $\text{PtSe}_2$  heterostructures are made up of  $\sqrt{10} \times \sqrt{5}$  cubic phases  $\text{Cs}_2\text{PbCl}_4$  and  $5 \times \sqrt{13}$   $\text{PtSe}_2$ ,  $\sqrt{10} \times \sqrt{5}$  cubic phases  $\text{Cs}_2\text{PbBr}_4$  and  $5 \times \sqrt{13}$   $\text{PtSe}_2$ , and  $\sqrt{8} \times 2$  cubic phases  $\text{Cs}_2\text{PbI}_4$  and  $5 \times \sqrt{13}$   $\text{PtSe}_2$ , as shown in Fig. 1. The maximum lattice mismatches of the 2D  $\text{Cs}_2\text{PbCl}_4$ – $\text{PtSe}_2$ ,  $\text{Cs}_2\text{PbBr}_4$ – $\text{PtSe}_2$  and  $\text{Cs}_2\text{PbI}_4$ – $\text{PtSe}_2$  heterostructures are 3.66%, 1.27% and 3.67%. The interface binding energy of  $\text{Cs}_2\text{PbCl}_4$ – $\text{PtSe}_2$ ,  $\text{Cs}_2\text{PbBr}_4$ – $\text{PtSe}_2$  and  $\text{Cs}_2\text{PbI}_4$ – $\text{PtSe}_2$  interfaces is −7.78, −46.07 and −15.34 meV Å<sup>−2</sup>, respectively. By comparing the interface binding energy of the above six models, we find that the positive correlation between the lattice mismatch and interface binding energy. With the lattice mismatch decreases, the interface binding energy of heterostructures decreases.

$\text{Cs}_2\text{PbX}_4$ – $\text{PtSe}_2$  heterostructures with smaller lattice mismatches are more stable due to the lower interface binding energy. Based on the stability, we chose the  $\text{Cs}_2\text{PbX}_4$ – $\text{PtSe}_2$  heterostructures with smaller lattice mismatches to study their electronic properties and optical properties.

To investigate the electronic properties and band alignments of 2D  $\text{Cs}_2\text{PbX}_4$ – $\text{PtSe}_2$  heterostructures, we firstly studied electronic structures of the monolayer  $\text{Cs}_2\text{PbX}_4$  and  $\text{PtSe}_2$ . The band gaps of the monolayer  $\text{Cs}_2\text{PbX}_4$  and  $\text{PtSe}_2$  are calculated by PBE, HSE, PBE with SOC (PBE + SOC) and HSE with SOC (HSE + SOC) functionals for comparison, the results are presented in Fig. S2 and Table S1.† It is shown that the band gaps calculated by HSE + SOC and PBE are very close to each other, while the band gap calculated by HSE is larger than PBE and the band gap calculated by PBE + SOC is smaller than PBE, which is consistent with earlier calculations on lead halide perovskites.<sup>50</sup> The band gaps of monolayer  $\text{Cs}_2\text{PbCl}_4$ ,  $\text{Cs}_2\text{PbBr}_4$  and  $\text{Cs}_2\text{PbI}_4$  by PBE functional are 2.59 eV, 2.18 eV and 1.84 eV, which are in good agreement with the theoretical and experimental band gaps of monolayer

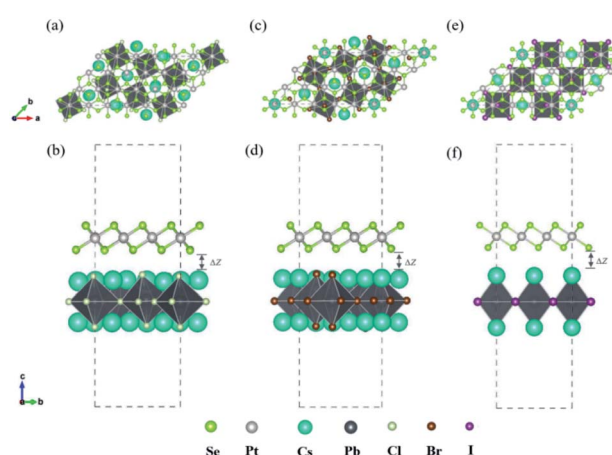


**Fig. 1** Top and side views of relaxed 45°  $\text{Cs}_2\text{PbX}_4$ – $\text{PtSe}_2$  heterostructures. (a and b)  $\text{Cs}_2\text{PbCl}_4$ – $\text{PtSe}_2$  heterostructure. (c and d)  $\text{Cs}_2\text{PbBr}_4$ – $\text{PtSe}_2$  heterostructure. (e and f)  $\text{Cs}_2\text{PbI}_4$ – $\text{PtSe}_2$  heterostructure. The unit cell of  $\text{Cs}_2\text{PbX}_4$ – $\text{PtSe}_2$  heterostructures are made up of  $\sqrt{10} \times \sqrt{5}$  cubic phases  $\text{Cs}_2\text{PbCl}_4$  and  $5 \times \sqrt{13}$   $\text{PtSe}_2$ ,  $\sqrt{10} \times \sqrt{5}$  cubic phases  $\text{Cs}_2\text{PbBr}_4$  and  $5 \times \sqrt{13}$   $\text{PtSe}_2$ , and  $\sqrt{8} \times 2$  cubic phases  $\text{Cs}_2\text{PbI}_4$  and  $5 \times \sqrt{13}$   $\text{PtSe}_2$ , as shown in figure.



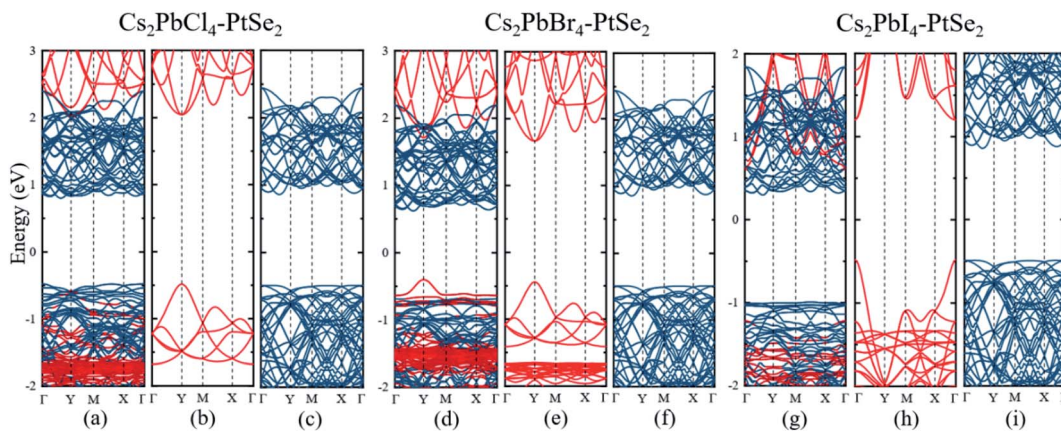


Fig. 2 Electronic band structures of  $\text{Cs}_2\text{PbX}_4$ – $\text{PtSe}_2$  heterostructures and corresponding monolayer  $\text{Cs}_2\text{PbX}_4$  and  $\text{PtSe}_2$ : (a–c)  $\text{X} = \text{Cl}$ ; (d–f)  $\text{X} = \text{Br}$ ; (g–i)  $\text{X} = \text{I}$ . The red and blue lines correspond to  $\text{Cs}_2\text{PbX}_4$  and  $\text{PtSe}_2$ , respectively. We calculated the electronic band structures of the  $\text{Cs}_2\text{PbX}_4$ – $\text{PtSe}_2$  heterostructures by PBE functional.

$\text{Cs}_2\text{PbX}_4$ .<sup>7,10,14,51</sup> In addition, the band gap of the  $\text{PtSe}_2$  monolayer using calculations PBE, HSE and HSE + SOC are 1.38 eV, 1.96 eV and 1.79 eV, respectively. Monolayer 1T- $\text{PtSe}_2$  has an indirect bandgap of 1.2 eV measured experimentally with ARPES, which is more consistent with the PBE and PBE + SOC results.<sup>30,52</sup> After comprehensive consideration, we apply PBE functional for further investigation.

Next, we calculated the electronic band structures of the  $\text{Cs}_2\text{PbX}_4$ – $\text{PtSe}_2$  heterostructures by PBE functional, as shown in Fig. 2(a), (d) and (g). The conduction band minimum (CBM) of  $\text{Cs}_2\text{PbX}_4$ – $\text{PtSe}_2$  heterostructures depends on  $\text{PtSe}_2$ , while the valence band maximum (VBM) depends on  $\text{PtSe}_2$  for  $\text{Cs}_2\text{PbCl}_4$ – $\text{PtSe}_2$  and  $\text{Cs}_2\text{PbI}_4$ – $\text{PtSe}_2$  heterostructures and  $\text{Cs}_2\text{PbBr}_4$  for  $\text{Cs}_2\text{PbBr}_4$ – $\text{PtSe}_2$  heterostructure. The band edges of  $\text{Cs}_2\text{PbX}_4$ – $\text{PtSe}_2$  heterojunctions are not equal to direct superposition of corresponding independent monolayer  $\text{Cs}_2\text{PbX}_4$  and  $\text{PtSe}_2$ , which are mainly induced by orbital coupling.<sup>53</sup> The CBM consists of d-orbital  $\text{PtSe}_2$  and the VBM consists of p and d orbital of  $\text{PtSe}_2$  and  $\text{Cs}_2\text{PbX}_4$ , as shown in Fig. S3.† The  $\text{Cs}_2\text{PbCl}_4$ – $\text{PtSe}_2$ ,  $\text{Cs}_2\text{PbBr}_4$ – $\text{PtSe}_2$  and  $\text{Cs}_2\text{PbI}_4$ – $\text{PtSe}_2$  heterostructures have an indirect bandgap with the value of 1.28 eV, 1.02 eV, and 1.29 eV, which approach optimal bandgap (1.34 eV) for solar cells.<sup>54</sup>

Furthermore, the Mott–Wannier theory has been used to approximate exciton binding energies in 2D.<sup>55</sup> The carrier masses and MW exciton binding energy of  $\text{Cs}_2\text{PbX}_4$ – $\text{PtSe}_2$  heterostructures are listed in Table 2. The lower carrier masses usually mean faster carrier transport.<sup>47</sup> Therefore,  $\text{Cs}_2\text{PbBr}_4$ – $\text{PtSe}_2$  heterostructure exhibit the highest hole and electron

mobility among  $\text{Cs}_2\text{PbX}_4$ – $\text{PtSe}_2$  heterostructures because it has the lowest  $m_e$  and  $m_h$ . In addition, small exciton binding energy facilitates the splitting of excitons into free charge carriers, indicating that  $\text{Cs}_2\text{PbBr}_4$ – $\text{PtSe}_2$  heterostructure can effectively promotes the separation of excitons.<sup>46</sup> Therefore,  $\text{Cs}_2\text{PbBr}_4$ – $\text{PtSe}_2$  heterostructure exhibits the highest charge transport efficiency among  $\text{Cs}_2\text{PbX}_4$ – $\text{PtSe}_2$  heterostructures.

In order to research energy level arrangement of  $\text{Cs}_2\text{PbX}_4$ – $\text{PtSe}_2$  heterostructures, we explored energy band in monolayer  $\text{Cs}_2\text{PbX}_4$  and  $\text{PtSe}_2$  from precontact (before contact) state to contact state. We set the vacuum level ( $E_v$ ) to zero in the precontact state and set the Fermi level ( $E_f$ ) to zero in the contact state to compare energy level heights of different heterostructures.<sup>56</sup> In the precontact state, the CBM and VBM of monolayer  $\text{Cs}_2\text{PbX}_4$  are both higher than that of monolayer  $\text{PtSe}_2$ , as shown in Fig. 3(a). The electrons will diffuse from the  $\text{Cs}_2\text{PbX}_4$  to the  $\text{PtSe}_2$  monolayer and the holes will move from the  $\text{PtSe}_2$  monolayer to the  $\text{Cs}_2\text{PbX}_4$  monolayer when they contact. Correspondingly, the holes accumulate in  $\text{Cs}_2\text{PbX}_4$  monolayer and the electrons accumulate in  $\text{PtSe}_2$  monolayer, leading to an increase of interface electric potential in  $\text{Cs}_2\text{PbX}_4$  monolayer and a decrease of this in  $\text{PtSe}_2$  monolayer.<sup>48,49</sup> Therefore, the band edges of  $\text{Cs}_2\text{PbX}_4$  interface are bent upward and those of  $\text{PtSe}_2$  interface are bent downward after the contact of monolayer  $\text{Cs}_2\text{PbX}_4$  and  $\text{PtSe}_2$ . The difference between the Fermi level and the vacuum level is defined as the work function, representing the binding capacity of electrons.<sup>56</sup> Calculated work functions of monolayers  $\text{Cs}_2\text{PbCl}_4$ ,  $\text{Cs}_2\text{PbBr}_4$ ,  $\text{Cs}_2\text{PbI}_4$  and  $\text{PtSe}_2$  are 4.08 eV, 4.21 eV, 4.30 eV, and 5.29 eV, respectively. Therefore, the Fermi level of all  $\text{Cs}_2\text{PbX}_4$  perovskites moved down and this of monolayer  $\text{PtSe}_2$  moved up after they contact each other, to keep the Fermi levels at the same level. The energy level diagram of  $\text{Cs}_2\text{PbX}_4$ – $\text{PtSe}_2$  heterostructures in the contact is shown in Fig. 3(b). The  $\text{Cs}_2\text{PbBr}_4$ – $\text{PtSe}_2$  heterostructure is type-II level alignment which is conducive to spontaneously drive the holes and electrons generated by the photoelectricity to move forward in opposite directions.<sup>48,49,57</sup> However, the  $\text{Cs}_2\text{PbCl}_4$ – $\text{PtSe}_2$  and  $\text{Cs}_2\text{PbI}_4$ – $\text{PtSe}_2$  heterostructures are type-I level alignment which is conducive to spontaneously drive the holes and electrons generated by the photoelectricity to move forward in opposite directions.<sup>48,49,57</sup>

Table 2 Carrier effective masses ( $m_e$ ,  $m_h$ , and  $\mu_{\text{ex}}$ ), static dielectric constant ( $\epsilon$ ), MW excitonic binding energies ( $E_{\text{eb}}$ )

Heterostructures	$m_e$ ( $m_0$ )	$m_h$ ( $m_0$ )	$\mu_{\text{ex}}$ ( $m_0$ )	$\epsilon$	$E_{\text{eb}}$ (eV)
$\text{Cs}_2\text{PbCl}_4$ – $\text{PtSe}_2$	0.36	4.87	0.34	5.42	0.62
$\text{Cs}_2\text{PbBr}_4$ – $\text{PtSe}_2$	0.34	0.44	0.19	5.55	0.34
$\text{Cs}_2\text{PbI}_4$ – $\text{PtSe}_2$	0.38	4.88	0.35	5.86	0.56



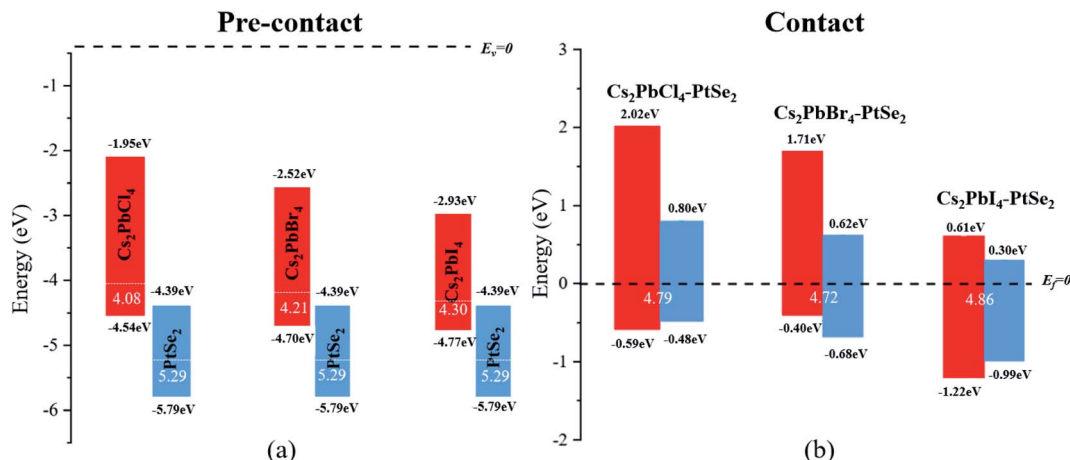


Fig. 3 Energy level graphs of the monolayer PtSe<sub>2</sub> and Cs<sub>2</sub>PbX<sub>4</sub> in the (a) precontact and (b) contact. Red and blue rectangles represent the monolayer Cs<sub>2</sub>PbX<sub>4</sub> and PtSe<sub>2</sub>. The bottom and top of rectangles correspond to VBM and CBM, respectively. The work function is labeled in the rectangles. In order to research energy level arrangement of Cs<sub>2</sub>PbX<sub>4</sub>–PtSe<sub>2</sub> heterostructures, we explored energy band in monolayer Cs<sub>2</sub>PbX<sub>4</sub> and PtSe<sub>2</sub> from precontact (before contact) state to contact state.

PtSe<sub>2</sub> heterostructures are type-I level arrangement. Due to the type-II level alignment of Cs<sub>2</sub>PbBr<sub>4</sub>–PtSe<sub>2</sub> heterostructure, it is useful to charge separation and improve PCE performance of Cs<sub>2</sub>PbX<sub>4</sub> solar cells.

In order to research the interfacial contact and charge transfer mechanism of Cs<sub>2</sub>PbX<sub>4</sub>–PtSe<sub>2</sub> heterostructures, plane-averaged charge density difference and corresponding 3D charge density difference were computed, as shown in Fig. 4. It is shown that electrons accumulate in PtSe<sub>2</sub> layer which is represented by blue region and the electrons dissipate in Cs<sub>2</sub>PbX<sub>4</sub> interface represented by red region, indicating that the electrons transfer from Cs<sub>2</sub>PbX<sub>4</sub> monolayer to the PtSe<sub>2</sub> monolayer. In addition, the holes primarily accumulate in the Cs<sub>2</sub>PbX<sub>4</sub> interface, revealing that the holes transfer from PtSe<sub>2</sub> monolayer to the Cs<sub>2</sub>PbX<sub>4</sub> monolayer. Besides, the amounts of

the charge transferring in the Cs<sub>2</sub>PbX<sub>4</sub>–PtSe<sub>2</sub> heterostructures follow the order Cl < Br < I, indicating Cs<sub>2</sub>PbI<sub>4</sub>–PtSe<sub>2</sub> and Cs<sub>2</sub>PbBr<sub>4</sub>–PtSe<sub>2</sub> heterostructures are more beneficial to interfacial charge transfer.

In order to further compare the charge transfers of the three heterojunctions, the plane-averaged electrostatic potentials of 2D Cs<sub>2</sub>PbX<sub>4</sub>–PtSe<sub>2</sub> heterostructures in the *z* direction are presented in Fig. 5. The electrostatic potentials drop from perovskites monolayer to PtSe<sub>2</sub> monolayer in the interfaces. The electrostatic potential difference values ( $\Delta EP$ , marked in Fig. 5) are involved in the charge transfers. A larger  $\Delta EP$  implies a powerful built-in electrostatic field which could lead to carrier dynamics and charge transfer.<sup>47,48</sup> The  $\Delta EP$  of Cs<sub>2</sub>PbCl<sub>4</sub>–PtSe<sub>2</sub>, Cs<sub>2</sub>PbBr<sub>4</sub>–PtSe<sub>2</sub> and Cs<sub>2</sub>PbI<sub>4</sub>–PtSe<sub>2</sub> heterostructures are 19.89 eV, 19.92 eV and 19.53 eV, respectively. Therefore, the

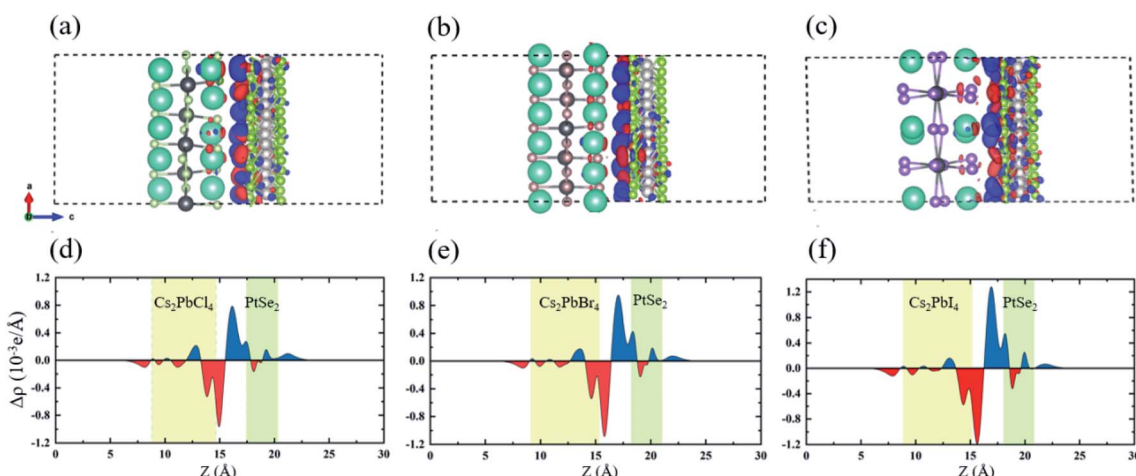


Fig. 4 3D charge density difference and corresponding planar-averaged differential charge density  $\Delta p(z)$  of Cs<sub>2</sub>PbX<sub>4</sub>–PtSe<sub>2</sub> heterostructures: (a and d) X = Cl; (b and e) X = Br; (c and f) X = I. Red and blue represent electron depletion and accumulation. The yellow and green areas represent Cs<sub>2</sub>PbX<sub>4</sub> and PtSe<sub>2</sub>, respectively. In order to research the interfacial contact and charge transfer mechanism of Cs<sub>2</sub>PbX<sub>4</sub>–PtSe<sub>2</sub> heterostructures, Plane-averaged charge density difference and corresponding 3D charge density difference were computed.



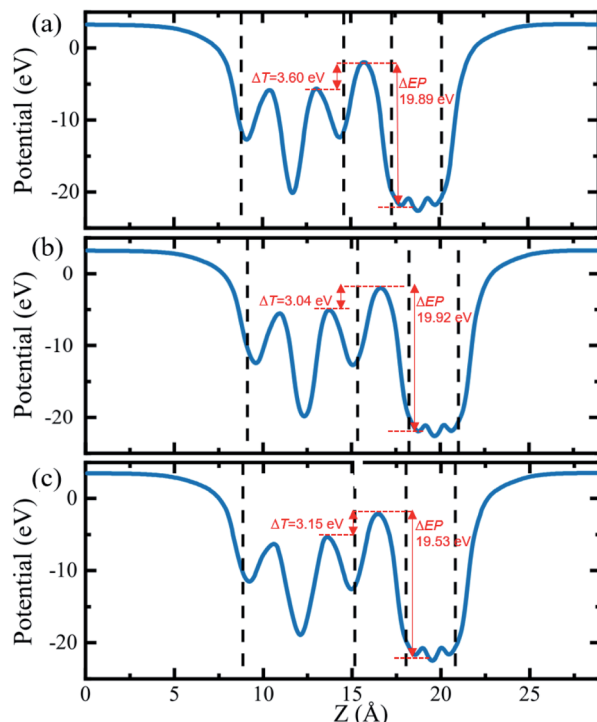


Fig. 5 The planar-averaged electrostatic potentials of  $\text{Cs}_2\text{PbX}_4$ – $\text{PtSe}_2$  heterostructures. (a)  $\text{Cs}_2\text{PbCl}_4$ – $\text{PtSe}_2$  heterostructure, (b)  $\text{Cs}_2\text{PbBr}_4$ – $\text{PtSe}_2$  heterostructure, (c)  $\text{Cs}_2\text{PbI}_4$ – $\text{PtSe}_2$  heterostructure. In order to further compare the charge transfers of the three heterojunctions, the plane-averaged electrostatic potentials of 2D  $\text{Cs}_2\text{PbX}_4$ – $\text{PtSe}_2$  heterostructures in the  $z$  direction are presented in figure.

$\text{Cs}_2\text{PbBr}_4$ – $\text{PtSe}_2$  heterostructure has the highest charge transfers in the three  $\text{Cs}_2\text{PbX}_4$ – $\text{PtSe}_2$  heterostructures due to the highest  $\Delta\text{EP}$ . In addition, tunnel barrier height ( $\Delta T$ , marked in Fig. 6) determines the electron transport efficiency, when the  $\Delta T$  is lower, the charge injection efficiency is higher.<sup>47</sup> The  $\Delta T$  of  $\text{Cs}_2\text{PbCl}_4$ – $\text{PtSe}_2$ ,  $\text{Cs}_2\text{PbBr}_4$ – $\text{PtSe}_2$  and  $\text{Cs}_2\text{PbI}_4$ – $\text{PtSe}_2$  heterostructures is 3.60 eV, 3.04 eV and 3.15 eV, respectively. Tunnel barrier height of  $\text{Cs}_2\text{PbBr}_4$ – $\text{PtSe}_2$  heterostructure is the lowest in the three  $\text{Cs}_2\text{PbX}_4$ – $\text{PtSe}_2$  heterostructures, so  $\text{Cs}_2\text{PbBr}_4$ – $\text{PtSe}_2$  heterostructure has the highest charge transport efficiency. From the above,  $\text{Cs}_2\text{PbBr}_4$ – $\text{PtSe}_2$  heterostructure has great potential for optoelectronic applications due to the highest  $\Delta\text{EP}$  and the lowest  $\Delta T$ .

The optical properties of perovskites have an important influence on the perovskite optoelectronic devices besides electronic structure. The optical absorption coefficients of single-layer  $\text{PtSe}_2$ , single-layer  $\text{Cs}_2\text{PbX}_4$ , and corresponding heterostructures were calculated, as represented in Fig. 6. The optical absorptions of all heterostructures are significantly greater than the corresponding monolayer  $\text{Cs}_2\text{PbX}_4$  and  $\text{PtSe}_2$ , which could be related to the interface contact of heterostructures. The light absorption coefficient of  $\text{Cs}_2\text{PbX}_4$ – $\text{MSe}_2$  heterostructures is at least twice higher than that of monolayer 2D inorganic halide perovskites. With the halogen varying from Cl to I, the light absorption coefficients of the  $\text{Cs}_2\text{PbX}_4$ – $\text{PtSe}_2$  heterostructures increase rapidly in the visible region. In the

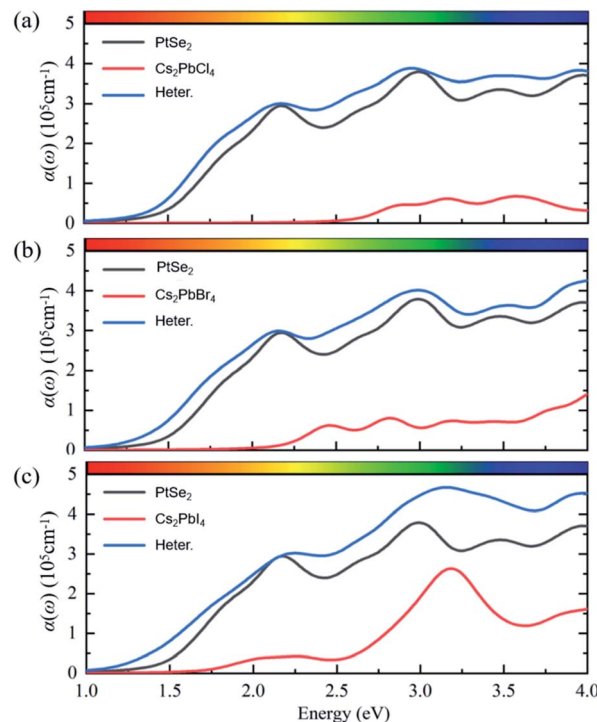


Fig. 6 The planar-averaged electrostatic potentials of  $\text{Cs}_2\text{PbX}_4$ – $\text{PtSe}_2$  heterostructures. (a)  $\text{Cs}_2\text{PbCl}_4$ – $\text{PtSe}_2$  heterostructure, (b)  $\text{Cs}_2\text{PbBr}_4$ – $\text{PtSe}_2$  heterostructure, (c)  $\text{Cs}_2\text{PbI}_4$ – $\text{PtSe}_2$  heterostructure. The optical properties of perovskites have an important influence on the perovskite optoelectronic devices besides electronic structure.

visible region, optical absorption spectra of  $\text{Cs}_2\text{PbI}_4$  is highest in the  $\text{Cs}_2\text{PbX}_4$  perovskites and the optical absorption spectra of  $\text{Cs}_2\text{PbCl}_4$  is lowest in the  $\text{Cs}_2\text{PbX}_4$  perovskites. The  $\text{Cs}_2\text{PbI}_4$ – $\text{PtSe}_2$  heterostructure shows the maximum optical absorption in visible regions. In addition, the optical absorption coefficients of single-layer  $\text{PtSe}_2$  are larger than those of 2D inorganic  $\text{Cs}_2\text{PbX}_4$  perovskites in the visible and ultraviolet regions. Therefore, building  $\text{PtSe}_2$  and 2D inorganic halide perovskite heterostructures would be an effective way to improve the optical absorption of 2D inorganic halide perovskite.

## Conclusions

In conclusion, we studied the structural, stability, optoelectronic properties and charge transfer mechanism of 2D halide perovskite heterostructures  $\text{Cs}_2\text{PbX}_4$ – $\text{PtSe}_2$  ( $\text{X} = \text{Cl}, \text{Br}, \text{I}$ ). Our results represent that 2D  $\text{Cs}_2\text{PbX}_4$ – $\text{PtSe}_2$  heterostructures are formed by van der Waals contact.  $\text{Cs}_2\text{PbCl}_4$ – $\text{PtSe}_2$ ,  $\text{Cs}_2\text{PbBr}_4$ – $\text{PtSe}_2$  and  $\text{Cs}_2\text{PbI}_4$ – $\text{PtSe}_2$  heterostructures have an indirect bandgap with the value of 1.28 eV, 1.02 eV, and 1.29 eV, respectively, which approach optimal bandgap (1.34 eV) for solar cells. In the precontact state, all the  $\text{Cs}_2\text{PbX}_4$ – $\text{PtSe}_2$  heterostructures exhibit type-II band arrangement, which drives the spontaneous motion of the carrier. In the contact state,  $\text{Cs}_2\text{PbBr}_4$ – $\text{PtSe}_2$  exhibits type-II band arrangement, while heterojunctions  $\text{Cs}_2\text{PbCl}_4$ – $\text{PtSe}_2$  and  $\text{Cs}_2\text{PbI}_4$ – $\text{PtSe}_2$  exhibit type-I band alignment. The charge density difference confirms that



the holes transfer from  $\text{PtSe}_2$  monolayer to the  $\text{Cs}_2\text{PbX}_4$  monolayer and the electrons transfer from  $\text{Cs}_2\text{PbX}_4$  monolayer to  $\text{PtSe}_2$  monolayer. Furthermore, the  $\text{Cs}_2\text{PbBr}_4\text{-PtSe}_2$  heterostructure has the highest electron transport efficiency due to the highest  $\Delta\text{EP}$  and the lowest  $\Delta T$ . In addition, the light absorption coefficient of  $\text{Cs}_2\text{PbX}_4\text{-MSe}_2$  heterostructures is at least twice higher than that of monolayer 2D inorganic halide perovskites. In summary, the construction of 2D inorganic halide perovskites and monolayer  $\text{PtSe}_2$  heterostructures is a useful method to enhance the optoelectronic performance of 2D inorganic halide perovskites for optoelectronic and photovoltaic applications.

## Conflicts of interest

There are no conflicts to declare.

## Acknowledgements

This work is supported by the Fund of State Key Laboratory of IPOC(BUPT) (No. IPOC2019ZZ04) and the Open-Foundation of Key Laboratory of Laser Device Technology, China North Industries Group Corporation Limited (Grant No. KLLDT202103). We thank for the helpful discussion with Prof. Pengfei Guan and the computational support from the Beijing Computational Science Research Center (CSRC).

## Notes and references

- 1 A. T. Barrows, A. J. Pearson, C. K. Kwak, A. D. F. Dunbar, A. R. Buckley and D. G. Lidzey, *Energy Environ. Sci.*, 2014, **7**, 2944–2950.
- 2 Y.-H. Kim, G.-H. Lee, Y.-T. Kim, C. Wolf, H. J. Yun, W. Kwon, C. G. Park and T. W. Lee, *Nano Energy*, 2017, **38**, 51–58.
- 3 J. Lu, A. Carvalho, H. Liu, S. X. Lim, A. H. Castro Neto and C. H. Sow, *Angew. Chem., Int. Ed.*, 2016, **55**, 11945–11949.
- 4 A. Kojima, K. Teshima, Y. Shirai and T. Miyasaka, *J. Am. Chem. Soc.*, 2009, **131**, 6050–6051.
- 5 K. Xiao, R. Lin, Q. Han, Y. Hou, Z. Qin, H. T. Nguyen, J. Wen, M. Wei, V. Yeddu, M. I. Saidaminov, Y. Gao, X. Luo, Y. Wang, H. Gao, C. Zhang, J. Xu, J. Zhu, E. H. Sargent and H. Tan, *Nat. Energy*, 2020, **5**, 870–880.
- 6 J. H. Noh, S. H. Im, J. H. Heo, T. N. Mandal and S. I. Seok, *Nano Lett.*, 2013, **13**, 1764–1769.
- 7 P. B. Gui, H. Zhou, F. Yao, Z. H. Song, B. R. Li and G. J. Fang, *Small*, 2019, **15**, DOI: 10.1002/smll.201902618.
- 8 H. Feng, C. C. Stoumpos, P. Guo, N. Zhou, T. J. Marks, R. P. H Chang and M. G. Kanatzidis, *J. Am. Chem. Soc.*, 2015, **137**, 11445–11452.
- 9 L. Wu, P. Lu, Y. Li, Y. Sun, J. Wong and K. Yang, *J. Mater. Chem. A*, 2018, **6**, 24389–24396.
- 10 Y. H. Li and K. S. Yang, *Energy Environ. Sci.*, 2019, **12**, 2233–2243.
- 11 Y. Li, D. Maldonado-Lopez, V. R. Vargas, J. Zhang and K. Yang, *J. Chem. Phys.*, 2020, **152**, 084106.
- 12 S. Chen and G. Shi, *Adv. Mater.*, 2017, **29**, DOI: 10.1002/adma.201605448.
- 13 A. Bala, A. K. Deb and V. Kumar, *J. Phys. Chem. C*, 2018, **122**, 7464–7473.
- 14 J. Song, L. Xu, J. Li, J. Xue, Y. Dong, X. Li and H. Zeng, *Adv. Mater.*, 2016, **28**, 4861–4869.
- 15 J. C. Liu, S. Lin, K. Huang, C. Jia, Q. M. Wang, Z. W. Li, J. N. Song, Z. L. Liu, H. Y. Wang, M. Lei and H. Wu, *npj Flexible Electron.*, 2020, **4**, 10.
- 16 K. Bi, Q. M. Wang, J. C. Xu, L. H. Chen, C. W. Lan and M. Lei, *Adv. Opt. Mater.*, 2021, **9**, 2001474.
- 17 J. C. Xu, K. Bi, R. Zhang, Y. N. Hao, C. W. Lan, M.-M. Klaus, X. J. Zhai, Z. D. Zhang and S. G. H, *Research*, 2019, **2019**, 968621.
- 18 S. Lin, J. C. Liu, W. Z. Li, D. Wang, Y. Huang, C. Jia, Z. W. Li, H. Y. Wang, J. N. Song, Z. L. Liu, K. Huang, D. Zu, M. Lei, B. Hong and H. Wu, *Nano Lett.*, 2019, **19**, 6853–6861.
- 19 J. C. Xu, J. Q. Cao, M. H. Guo, S. L. Yang, H. M. Yao, M. Lei, Y. N. Hao and K. Bi, *Adv. Compos. Hybrid Mater.*, 2021, **4**, 761–767.
- 20 Q. M. Wang, J. M. Zhang, Z. D. Zhang, Y. N. Hao and K. Bi, *Adv. Compos. Hybrid Mater.*, 2020, **3**, 58–65.
- 21 B. N. Jia, P. F. Zhu, S. H. Sun, L. H. Han, G. Liu, Y. Wang, G. D. Peng and P. F. Lu, *J. Sichuan Norm. Univ., Nat. Sci.*, 2020, **26**, 1–6.
- 22 X. Song, X. Liu, D. Yu, C. Huo, J. Ji, X. Li, S. Zhang, Y. Zou, G. Zhu, Y. Wang, M. Wu, A. Xie and H. Zeng, *ACS Appl. Mater. Interfaces*, 2018, **10**, 2801–2809.
- 23 D. Wijethunge, L. Zhang, C. Tang and A. Du, *Front. Phys.*, 2020, **15**, 63504.
- 24 X. R. Hu, J. M. Zheng and Z. Y. Ren, *Front. Phys.*, 2018, **13**, 137302.
- 25 Z. P. Zhou, M. A. Springer, W. X. Geng, X. Y. Zhu, T. C. Li, M. M. Li, Y. Jing and T. Heine, *J. Phys. Chem. Lett.*, 2021, **12**, 8134–8140.
- 26 Y. Jing, Z. P. Zhou, W. X. Geng, X. Y. Zhu and T. Heine, *Adv. Mater.*, 2021, **33**, 2008645.
- 27 Y. Jing, Z. P. Zhou, J. Zhang, C. B. Huang, Y. F. Li and F. Wang, *Phys. Chem. Chem. Phys.*, 2019, **21**, 21064–21069.
- 28 Y. Choi, S. Jung, N. K. Oh, J. Lee, J. Seo, U. Kim, D. Koo and H. Park, *Chemnanomat*, 2019, **5**, 1050–1058.
- 29 Y. Wang, L. Li, W. Yao, S. Song, J. T. Sun, J. Pan, X. Ren, C. Li, E. Okunishi, Y.-Q. Wang, E. Wang, Y. Shao, Y. Y. Zhang, H.-t. Yang, E. F. Schwier, H. Iwasawa, K. Shimada, M. Taniguchi, Z. Cheng, S. Zhou, S. Du, S. J. Pennycook, S. T. Pantelides and H.-J. Gao, *Nano Lett.*, 2015, **15**, 4013–4018.
- 30 R. A. B. Villaos, C. P. Crisostomo, Z.-Q. Huang, S.-M. Huang, A. A. B. Padama, M. A. Albao, H. Lin and F.-C. Chuang, *npj 2D Mater. Appl.*, 2019, **3**, DOI: 10.1038/s41699-018-0085-z.
- 31 Y. Zhao, J. Qiao, Z. Yu, P. Yu, K. Xu, S. P. Lau, W. Zhou, Z. Liu, X. Wang, W. Ji and Y. Chai, *Adv. Mater.*, 2017, **29**, DOI: 10.1002/adma.201604230.
- 32 A. Ciarrocchi, A. Avsar, D. Ovchinnikov and A. Kis, *Nat. Commun.*, 2018, **9**, DOI: 10.1038/s41467-018-03436-0.
- 33 L.-H. Zeng, S.-H. Lin, Z.-J. Li, Z.-X. Zhang, T.-F. Zhang, C. Xie, C.-H. Mak, Y. Chai, S. P. Lau, L.-B. Luo and Y. H. Tsang, *Adv. Funct. Mater.*, 2018, **28**, DOI: 10.1002/adfm.201705970.



34 Z. X. Zhang, L. H. Zeng, X. W. Tong, Y. Gao, C. Xie, Y. H. Tsang, L. B. Luo and Y. C. Wu, *J. Phys. Chem. Lett.*, 2018, **9**, 1185–1194.

35 P. E. Blochl, *Phys. Rev. B: Condens. Matter Mater. Phys.*, 1994, **50**, 17953–17979.

36 G. Kresse and D. Joubert, *Phys. Rev. B: Condens. Matter Mater. Phys.*, 1999, **59**, 1758–1775.

37 J. P. Perdew, K. Burke and M. Ernzerhof, *Phys. Rev. Lett.*, 1996, **77**, 3865–3868.

38 X. N. Guan, R. Zhang, B. N. Jia, L. Y. Wu, B. Zhou, L. Fan, G. Liu, Y. Wang, P. F. Lu and G. D. Peng, *J. Non-Cryst. Solids*, 2020, **550**, 120388.

39 B. Liu, M. Long, M.-Q. Cai and J. Yang, *Appl. Phys. Lett.*, 2018, **112**, 043901.

40 J. Heyd, G. E. Scuseria and M. Ernzerhof, *J. Chem. Phys.*, 2003, **118**, 8207–8215.

41 P. Z. B. Jia, S. Sun, L. Han, G. Liu, Y. Wang, G.-D. Peng and P. Lu, *IEEE J. Sel. Top. Quantum Electron.*, 2019, **26**, 1–6.

42 A. Molina-Sanchez, *ACS Appl. Energy Mater.*, 2018, **1**, 6361–6367.

43 J.-H. Yang, Q. Yuan and B. I. Yakobson, *J. Phys. Chem. C*, 2016, **120**, 24682–24687.

44 J. Haruyama, K. Sodeyama, L. Han and Y. Tateyama, *J. Phys. Chem. Lett.*, 2014, **5**, 2903–2909.

45 D.-J. Yang, Y.-H. Du, Y.-Q. Zhao, Z.-L. Yu and M.-Q. Cai, *Phys. Status Solidi B*, 2019, **256**, DOI: 10.1002/pssb.201800540.

46 J. H. Chen, X. J. He, B. S. Sa, J. Zhou, C. Xu, C. L. Wen and Z. M. Sun, *Nanoscale*, 2019, **11**, 6431–6444.

47 J. He, J. Su, Z. Lin, S. Zhang, Y. Qin, J. Zhang, J. Chang and Y. Hao, *J. Phys. Chem. C*, 2019, **123**, 7158–7165.

48 Y.-Q. Zhao, Y. Xu, D.-F. Zou, J.-N. Wang, G.-F. Xie, B. Liu, M.-Q. Cai and S.-L. Jiang, *J. Phys.: Condens. Matter*, 2020, **32**, 19.

49 B. Liu, M. Long, M.-Q. Cai and J. Yang, *J. Phys. Chem. Lett.*, 2018, **9**, 4822–4827.

50 W. J. Yin, J. H. Yang, J. Kang, Y. Yan and S. H. Wei, *J. Mater. Chem. A*, 2015, **3**, 8926–8942.

51 P. B. Gui, H. Zhou, F. Yao, Z. H. Song, B. R. Li and G. J. Fang, *Small*, 2019, **15**, DOI: 10.1002/adom.201800879.

52 L. Fang, W. Liang, Q. Feng and S.-N. Luo, *J. Phys.: Condens. Matter*, 2019, **31**, 455001.

53 Y. Si, H. Y. Wu, K. Yang, J. C. Lian, T. Huang, W. Q. Huang, W. Y. Hu and G. F. Huang, *Appl. Phys. Lett.*, 2021, **119**, 043102.

54 S. Ruhle, *Sol. Energy*, 2016, **130**, 139–147.

55 P. Wang, Y. X. Zong, H. Liu, H. Y. Wen, H. X. Deng, Z. M. Wei, H. B. Wu and J. B. Xia, *J. Phys. Chem. C*, 2020, **214**, 23832–23838.

56 B. Liu, Y.-Q. Zhao, Z.-L. Yu, L.-Z. Wang and M.-Q. Cai, *J. Colloid Interface Sci.*, 2018, **513**, 677–683.

57 W. Niu, A. Eiden, G. V. Prakash and J. J. Baumberg, *Appl. Phys. Lett.*, 2014, **104**, 171111.

